



# Interferometric near-infrared spectroscopy (iNIRS): performance tradeoffs and optimization

OYBEK KHOLIQOV,<sup>1</sup> DAWID BORYCKI,<sup>1,2</sup> AND VIVEK J. SRINIVASAN<sup>1,3,\*</sup>

<sup>1</sup>Department of Biomedical Engineering, University of California Davis, CA 95616, USA

<sup>2</sup>Present address: Institute of Physical Chemistry, Polish Academy of Sciences, Kasprzaka 44/52, 01-224 Warsaw, Poland

<sup>3</sup>Department of Ophthalmology and Vision Science, University of California Davis, Davis School of Medicine, Sacramento, CA 96817, USA

\*[vjsriniv@ucdavis.edu](mailto:vjsriniv@ucdavis.edu)

**Abstract:** Interferometric near-infrared spectroscopy (iNIRS) is a time-of-flight- (TOF-) resolved sensing modality for determining optical and dynamical properties of a turbid medium. iNIRS achieves this by measuring the interference spectrum of light traversing the medium with a rapidly tunable, or frequency-swept, light source. Thus, iNIRS system performance critically depends on the source and detection apparatus. Using a current-tuned 855 nm distributed feedback laser as the source, we experimentally characterize iNIRS system parameters, including speed, sensitivity, dynamic range, TOF resolution, and TOF range. We also employ a novel Mach-Zehnder interferometer variant with a multi-pass loop to monitor the laser instantaneous linewidth and TOF range at high tuning speeds. We identify and investigate tradeoffs between parameters, with the goal of optimizing performance. We also demonstrate a technique to combine forward and backward sweeps to double the effective speed. Combining these advances, we present *in vivo* TPSFs and autocorrelations from the mouse brain with TOF resolutions of 22-60 ps, 36-47 dB peak-sidelobe dynamic range, 4-10  $\mu$ s autocorrelation lag time resolution, a TOF range of nanoseconds or more, and nearly shot noise limited sensitivity.

© 2017 Optical Society of America

**OCIS codes:** (030.1640) Coherence; (140.3600) Lasers, tunable; (140.3490) Lasers, distributed-feedback; (160.4760) Optical properties; (170.7050) Turbid media; (170.4500) Optical coherence tomography; (290.4210) Multiple scattering; (170.6920) Time-resolved imaging; (170.6480) Spectroscopy, speckle.

## References and links

1. F. F. Jobsis, "Noninvasive, infrared monitoring of cerebral and myocardial oxygen sufficiency and circulatory parameters," *Science* **198**(4323), 1264–1267 (1977).
2. A. Torricelli, D. Contini, A. Pifferi, M. Caffini, R. Re, L. Zucchelli, and L. Spinelli, "Time domain functional NIRS imaging for human brain mapping," *Neuroimage* **85**(Pt 1), 28–50 (2014).
3. S. Fantini, M. A. Franceschini, J. B. Fishkin, B. Barbieri, and E. Gratton, "Quantitative determination of the absorption spectra of chromophores in strongly scattering media: a light-emitting-diode based technique," *Appl. Opt.* **33**(22), 5204–5213 (1994).
4. D. A. Boas and M. A. Franceschini, "Haemoglobin oxygen saturation as a biomarker: the problem and a solution," *Philos. Trans. A Math Phys. Eng. Sci.* **369**, 4407–4424 (2011).
5. T. Durduran and A. G. Yodh, "Diffuse correlation spectroscopy for non-invasive, micro-vascular cerebral blood flow measurement," *Neuroimage* **85**(Pt 1), 51–63 (2014).
6. T. Durduran, R. Choe, W. B. Baker, and A. G. Yodh, "Diffuse optics for tissue monitoring and tomography," *Rep. Prog. Phys.* **73**(7), 076701 (2010).
7. N. Roche-Labarbe, A. Fenoglio, H. Radhakrishnan, M. Kocienski-Filip, S. A. Carp, J. Dubb, D. A. Boas, P. E. Grant, and M. A. Franceschini, "Somatosensory evoked changes in cerebral oxygen consumption measured non-invasively in premature neonates," *Neuroimage* **85**(Pt 1), 279–286 (2014).
8. V. Jain, E. M. Buckley, D. J. Licht, J. M. Lynch, P. J. Schwab, M. Y. Naim, N. A. Lavin, S. C. Nicolson, L. M. Montenegro, A. G. Yodh, and F. W. Wehrli, "Cerebral oxygen metabolism in neonates with congenital heart disease quantified by MRI and optics," *J. Cereb. Blood Flow Metab.* **34**(3), 380–388 (2014).
9. F. Scholkmann, S. Kleiser, A. J. Metz, R. Zimmermann, J. Mata Pavia, U. Wolf, and M. Wolf, "A review on continuous wave functional near-infrared spectroscopy and imaging instrumentation and methodology," *Neuroimage* **85**(Pt 1), 6–27 (2014).

10. M. Ferrari and V. Quaresima, "A brief review on the history of human functional near-infrared spectroscopy (fNIRS) development and fields of application," *Neuroimage* **63**(2), 921–935 (2012).
11. M. Smith, "Shedding light on the adult brain: a review of the clinical applications of near-infrared spectroscopy," *Philos. Trans. A Math Phys. Eng. Sci.* **369**, 4452–4469 (2011).
12. D. Borycki, O. Kholiqov, S. P. Chong, and V. J. Srinivasan, "Interferometric Near-Infrared Spectroscopy (iNIRS) for determination of optical and dynamical properties of turbid media," *Opt. Express* **24**(1), 329–354 (2016).
13. D. Borycki, O. Kholiqov, and V. J. Srinivasan, "Interferometric near-infrared spectroscopy directly quantifies optical field dynamics in turbid media," *Optica* **3**(12), 1471–1476 (2016).
14. D. Borycki, O. Kholiqov, and V. J. Srinivasan, "Reflectance-mode interferometric near-infrared spectroscopy quantifies brain absorption, scattering, and blood flow index in vivo," *Opt. Lett.* **42**(3), 591–594 (2017).
15. A. Kienle and M. S. Patterson, "Improved solutions of the steady-state and the time-resolved diffusion equations for reflectance from a semi-infinite turbid medium," *J. Opt. Soc. Am. A* **14**(1), 246–254 (1997).
16. S. M. Kazmi, R. K. Wu, and A. K. Dunn, "Evaluating multi-exposure speckle imaging estimates of absolute autocorrelation times," *Opt. Lett.* **40**(15), 3643–3646 (2015).
17. D. J. Pine, D. A. Weitz, P. M. Chaikin, and E. Herbolzheimer, "Diffusing wave spectroscopy," *Phys. Rev. Lett.* **60**(12), 1134–1137 (1988).
18. M. Wojtkowski, V. Srinivasan, T. Ko, J. Fujimoto, A. Kowalczyk, and J. Duker, "Ultra-high-resolution, high-speed, Fourier domain optical coherence tomography and methods for dispersion compensation," *Opt. Express* **12**(11), 2404–2422 (2004).
19. S. H. Yun, C. Boudoux, G. J. Tearney, and B. E. Bouma, "High-speed wavelength-swept semiconductor laser with a polygon-scanner-based wavelength filter," *Opt. Lett.* **28**(20), 1981–1983 (2003).
20. S. W. C. Larry, A. Coldren, *Diode Lasers and Photonic Integrated Circuits*, 2nd ed. (2012).
21. M. Choma, M. Sarunic, C. Yang, and J. Izatt, "Sensitivity advantage of swept source and Fourier domain optical coherence tomography," *Opt. Express* **11**(18), 2183–2189 (2003).
22. R. Leitgeb, C. Hitzenberger, and A. Fercher, "Performance of fourier domain vs. time domain optical coherence tomography," *Opt. Express* **11**(8), 889–894 (2003).
23. J. Sutin, B. Zimmerman, D. Tyulmankov, D. Tamborini, K. C. Wu, J. Selb, A. Gulinatti, I. Rech, A. Tosi, D. A. Boas, and M. A. Franceschini, "Time-domain diffuse correlation spectroscopy," *Optica* **3**(9), 1006–1013 (2016).
24. J. F. de Boer, B. Cense, B. H. Park, M. C. Pierce, G. J. Tearney, and B. E. Bouma, "Improved signal-to-noise ratio in spectral-domain compared with time-domain optical coherence tomography," *Opt. Lett.* **28**(21), 2067–2069 (2003).
25. A. Torricelli, A. Pifferi, L. Spinelli, R. Cubeddu, F. Martelli, S. Del Bianco, and G. Zaccanti, "Time-resolved reflectance at null source-detector separation: improving contrast and resolution in diffuse optical imaging," *Phys. Rev. Lett.* **95**(7), 078101 (2005).
26. A. Pifferi, A. Torricelli, L. Spinelli, D. Contini, R. Cubeddu, F. Martelli, G. Zaccanti, A. Tosi, A. Dalla Mora, F. Zappa, and S. Cova, "Time-resolved diffuse reflectance using small source-detector separation and fast single-photon gating," *Phys. Rev. Lett.* **100**(13), 138101 (2008).
27. T. Butler, S. Slepneva, B. O'Shaughnessy, B. Kelleher, D. Goulding, S. P. Hegarty, H.-C. Lyu, K. Karnowski, M. Wojtkowski, and G. Huyet, "Single shot, time-resolved measurement of the coherence properties of OCT swept source lasers," *Opt. Lett.* **40**(10), 2277–2280 (2015).
28. M. S. Patterson, B. Chance, and B. C. Wilson, "Time resolved reflectance and transmittance for the non-invasive measurement of tissue optical properties," *Appl. Opt.* **28**(12), 2331–2336 (1989).
29. A. J. Lin, M. A. Koike, K. N. Green, J. G. Kim, A. Mazhar, T. B. Rice, F. M. LaFerla, and B. J. Tromberg, "Spatial frequency domain imaging of intrinsic optical property contrast in a mouse model of Alzheimer's disease," *Ann. Biomed. Eng.* **39**(4), 1349–1357 (2011).
30. A. J. Lin, N. A. Castello, G. Lee, K. N. Green, A. J. Durkin, B. Choi, F. LaFerla, and B. J. Tromberg, "In vivo optical signatures of neuronal death in a mouse model of Alzheimer's disease," *Lasers Surg. Med.* **46**(1), 27–33 (2014).
31. M. Buttafava, E. Martinenghi, D. Tamborini, D. Contini, A. D. Mora, M. Renna, A. Torricelli, A. Pifferi, F. Zappa, and A. Tosi, "A compact two-wavelength time-domain NIRS system based on SiPM and pulsed diode lasers," *IEEE Photonics J.* **9**(1), 1–14 (2017).
32. "nanoplus | Distributed Feedback Lasers: 760 nm - 830 nm," <http://nanoplus.com/en/products/distributed-feedback-lasers/distributed-feedback-lasers-760-nm-830-nm/>.
33. M. Bonesi, M. P. Minneman, J. Ensher, B. Zabihian, H. Sattmann, P. Boschert, E. Hoover, R. A. Leitgeb, M. Crawford, and W. Drexler, "Akinetic all-semiconductor programmable swept-source at 1550 nm and 1310 nm with centimeters coherence length," *Opt. Express* **22**(3), 2632–2655 (2014).
34. N. Fujiwara, R. Yoshimura, K. Kato, H. Ishii, F. Kano, Y. Kawaguchi, Y. Kondo, K. Ohbayashi, and H. Oohashi, "140-nm Quasi-Continuous Fast Sweep Using SSG-DBR Lasers," *IEEE Photonics Technol. Lett.* **20**(12), 1015–1017 (2008).
35. Laser Institute of America, *ANSI Z136.1*, American National Standard for Safe Use of Lasers (n.d.).
36. T. Pfeiffer, W. Wieser, T. Klein, M. Petermann, J.-P. Kolb, M. Eibl, and R. Huber, "Flexible A-scan rate MHz OCT: Computational downscaling by coherent averaging," *Proc. SPIE* **9697**, 96970S (2016).

37. A. Tosi, A. D. Mora, F. Zappa, A. Gulinatti, D. Contini, A. Pifferi, L. Spinelli, A. Torricelli, and R. Cubeddu, "Fast-gated single-photon counting technique widens dynamic range and speeds up acquisition time in time-resolved measurements," *Opt. Express* **19**(11), 10735–10746 (2011).
38. H. Wabnitz, D. R. Taubert, M. Mazurenka, O. Steinkellner, A. Jelzow, R. Macdonald, D. Milej, P. Sawosz, M. Kacprzak, A. Liebert, R. Cooper, J. Hebden, A. Pifferi, A. Farina, I. Bargigia, D. Contini, M. Caffini, L. Zucchelli, L. Spinelli, R. Cubeddu, and A. Torricelli, "Performance assessment of time-domain optical brain imagers, part 1: basic instrumental performance protocol," *J. Biomed. Opt.* **19**(8), 086010 (2014).
39. D. Contini, A. D. Mora, L. Spinelli, A. Farina, A. Torricelli, R. Cubeddu, F. Martelli, G. Zaccanti, A. Tosi, G. Boso, F. Zappa, and A. Pifferi, "Effects of time-gated detection in diffuse optical imaging at short source-detector separation," *J. Phys. D Appl. Phys.* **48**(4), 045401 (2015).
40. K. K. Hamamatsu Photonics, (editorial committee), *Photomultiplier Tubes - Basics and Applications*, 3rd ed. (Hamamatsu Photonics, 2007).
41. S. Han, J. Johansson, M. Mireles, A. R. Proctor, M. D. Hoffman, J. B. Vella, D. S. W. Benoit, T. Durduran, and R. Choe, "Non-contact scanning diffuse correlation tomography system for three-dimensional blood flow imaging in a murine bone graft model," *Biomed. Opt. Express* **6**(7), 2695–2712 (2015).
42. G. Dietsche, M. Ninck, C. Ortoff, J. Li, F. Jaillon, and T. Gisler, "Fiber-based multispeckle detection for time-resolved diffusing-wave spectroscopy: characterization and application to blood flow detection in deep tissue," *Appl. Opt.* **46**(35), 8506–8514 (2007).

## 1. Introduction

The field of near-infrared spectroscopy (NIRS) aims to non-invasively probe the physiology of highly scattering biological tissues with near-infrared light [1]. Continuous wave (CW-) NIRS measures changes in the absorption coefficient at different wavelengths to assess oxyhemoglobin and deoxyhemoglobin concentration changes, but not baseline values. By adding additional dimensions to the measurement, time-domain (TD-) [2] and frequency-domain (FD-) [3] NIRS methods can quantify optical properties, enabling them to measure baseline hemoglobin concentration and saturation. However, oxygenation alone may be ambiguous without information about blood perfusion or flow [4]. To evaluate blood flow, Diffuse Correlation Spectroscopy (DCS) [5,6] analyzes temporal autocorrelations of coherent light, multiply scattered through tissue, to infer red blood cell dynamics. Equipped with flow, hemoglobin concentration, and oxygen saturation, multimodality NIRS-DCS instruments can monitor tissue metabolic rate of oxygen non-invasively [7,8]. Current challenges in the field of NIRS are 1) the large number of assumptions needed to quantify baseline flow and oxygenation from simple CW measurements, 2) the high cost of more accurate TD-NIRS and FD-NIRS methods, and 3) the need for complex multimodality instrumentation to perform flowmetry and oximetry simultaneously. A single NIRS modality to quantify both tissue optical properties and dynamics would both improve accuracy of NIRS and enhance its numerous applications [9–11].

Interferometric near-infrared spectroscopy (iNIRS) is a new time-of-flight (TOF-) resolved optical modality that can assess optical properties and dynamics with a single instrument. The theoretical iNIRS framework [12,13] and *in vivo* application [14] have been described previously. In this work, for the first time, we characterize and optimize the iNIRS setup with respect to speed, sensitivity, dynamic range, TOF resolution (related to laser tuning range), and TOF range (related to laser linewidth, sampling, and detection bandwidth). In doing so, we introduce a method for monitoring the instantaneous linewidth and coherence time of temporally coherent and rapidly tuned lasers, based on a novel multi-pass loop variant of a modified Mach-Zehnder interferometer. We show that both forward and backward sweeps nearly achieve the shot noise limit, and combine them to double the temporal sampling of the field autocorrelation. Finally, after accounting for tradeoffs to determine the system operating point, we show iNIRS TPSFs and autocorrelations *in vivo* at 2.3x higher TOF resolution and 5x higher autocorrelation time lag sampling than demonstrated previously [14].

## 2. iNIRS theory and system parameters

### 2.1 iNIRS theory

The theory for iNIRS is based on the TOF-resolved field autocorrelation [14]. The iNIRS method uses a tunable narrow-linewidth source to illuminate a turbid sample, and interferes the multiply scattered sample light with light traversing a reference path via a modified Mach-Zehnder interferometer (MZI), as shown in Fig. 1(a) [12]. The source tunes over optical wavelength ( $\lambda$ ) or frequency ( $\nu$ ). Fourier transformation of the spectral interference signal (resampled, if needed, to be uniformly spaced in  $\nu$ ) yields the mutual coherence function between sample and reference fields,  $\Gamma_{rs}(\tau_s, t_d)$ , which depends on TOF ( $\tau_s$ ) and delay time ( $t_d$ ). Incoherent averaging over  $t_d$  yields the temporal point spread function (TPSF),  $I^{iNIRS}(\tau_s)$ , where

$$I^{iNIRS}(\tau_s) = \left\langle |\Gamma_{rs}(\tau_s, t_d)|^2 \right\rangle_{t_d}. \quad (1)$$

The TPSF represents the intrinsic medium distribution of times-of-flight (DTOF),  $I(\tau_s)$ , convolved (\*) in TOF ( $\tau_s$ ) with the instrument response function (IRF),  $IRF(\tau_s)$ :

$$I^{iNIRS}(\tau_s) = I(\tau_s) * IRF(\tau_s). \quad (2)$$

TPSFs are then fitted with  $A \times [\mathfrak{R}(\tau_s) * IRF(\tau_s)]$ , where  $A$  is a scaling factor, and  $\mathfrak{R}(\tau_s)$  is the TOF-resolved diffusion approximation of reflectance from a semi-infinite medium [15], to extract absorption and reduced scattering coefficients:  $\mu_a$  and  $\mu_s'$ , respectively [14], by minimizing the norm-squared of the error:

$$\min_{(\mu_a, \mu_s', A)} \|A \times [\mathfrak{R}(\tau_s) * IRF(\tau_s)] - I^{iNIRS}(\tau_s)\|^2. \quad (3)$$

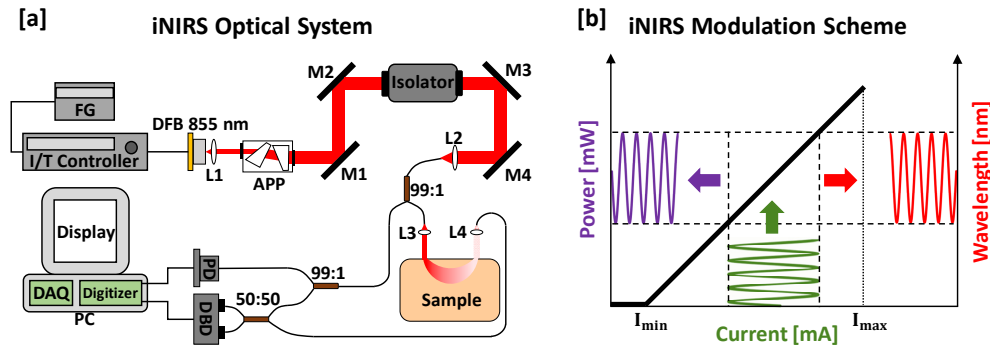


Fig. 1. iNIRS optical system and modulation scheme. a) The function generator (FG) sinusoidally modulates the injected drive current via the integrated current/temperature controller (I/T controller); the injected drive current in turn modulates the optical frequency of the distributed feedback laser (DFB). The laser output beam is collimated (L1), shaped with an anamorphic prism pair (APP), isolated (55 dB Thorlabs isolator), and finally coupled (L2) to a few mode fiber (SMF-28). M1-M4 are steering mirrors. The beam is split into reference (1%) and sample (99%) arms with a 99:1 fiber coupler, where the sample arm is collimated (L3) before illuminating the turbid medium. A single mode fiber coupler (L4) collects multiply scattered sample light, which is combined with the reference light by a 50:50 fiber coupler, before detection by a dual-balanced detector (DBD). Simultaneous reference power measurements are recorded with a photodiode (PD). Finally, iNIRS interference signals and reference power measurements are digitized and processed with a PC. b) This implementation of iNIRS relies on injection current modulation for wavelength tuning, resulting in concomitant modulation of the DFB laser output power as the wavelength is tuned.

Similarly, TOF-resolved, un-normalized iNIRS field autocorrelations,  $G_1^{\text{iNIRS}}(\tau_s, \tau_d)$ , are functions of both TOF ( $\tau_s$ ) and lag time ( $\tau_d$ ) [12,13]:

$$G_1^{\text{iNIRS}}(\tau_s, \tau_d) = \left\langle \Gamma_{\text{rs}}^*(\tau_s, t_d) \Gamma_{\text{rs}}(\tau_s, t_d + \tau_d) \right\rangle_{t_d}. \quad (4)$$

iNIRS autocorrelations are related to the intrinsic medium field autocorrelation,  $G_1(\tau_s, \tau_d)$ , by a convolution in TOF ( $\tau_s$ ) with the IRF:

$$G_1^{\text{iNIRS}}(\tau_s, \tau_d) = G_1(\tau_s, \tau_d) * \text{IRF}(\tau_s). \quad (5)$$

Thus, iNIRS provides the unique capability to measure TOF-resolved field autocorrelations. This capability enables more direct quantification of sample dynamics [12,14] than is possible with intensity autocorrelations [16]. In the Diffusing Wave Spectroscopy (DWS) regime [17], the normalized TOF-resolved field autocorrelation  $g_1(\tau_s, \tau_d)$  is given by:

$$g_1(\tau_s, \tau_d) = \frac{G_1(\tau_s, \tau_d)}{G_1(\tau_s, 0)} = \exp[-\xi(\tau_s)\tau_d] = \exp[-2k^2\alpha D_B \mu_s' L \tau_d], \quad (6)$$

where  $\xi(\tau_s) = 2k^2\alpha D_B \mu_s' c \tau_s / n$  is the TOF-resolved decay rate,  $L = c\tau_s/n$  is the photon path length,  $k = 2\pi n/\lambda_c$  is the medium wavenumber, and  $\alpha D_B = \text{BFI}$  is the blood flow index [5]. Provided that  $\mu_s'$  can be determined from Eq. (3), BFI can be straightforwardly determined [12].

Note that  $I^{\text{iNIRS}}(\tau_s) = G_1^{\text{iNIRS}}(\tau_s, 0)$  and  $I(\tau_s) = G_1(\tau_s, 0)$ ; hence Eq. (5) also implies Eq. (2). As convolution involves a smoothing along the TOF axis, iNIRS requires a fine TOF resolution to determine optical properties and TOF-resolved medium dynamics.

## 2.2 Tuning range determines time-of-flight resolution

The TOF resolution, or width of the IRF, is inversely related to the tuning range, or optical bandwidth, of the light source [12]. A fine TOF resolution causes the TPSF to better approximate the DTOF in Eq. (2), and improves TOF selectivity for recovering dynamics from the field autocorrelation in Eq. (5). We assume that  $\Delta\nu$  and  $\Delta\lambda$  are the laser full-width at half-maximum (FWHM) bandwidths in optical frequency and wavelength respectively,  $c$  is the speed of light in vacuum, and  $\lambda_c$  is the central wavelength. For a Gaussian spectrum, the theoretical FWHM TOF resolution,  $\delta\tau_s$ , is given by

$$\delta\tau_s = \frac{2\sqrt{2}\ln(2)}{\pi\Delta\nu} = \frac{2\sqrt{2}\ln(2)\lambda_c^2}{\pi c\Delta\lambda}. \quad (7)$$

In reality, it is not possible to achieve a perfectly Gaussian spectrum as the tuning range is finite, and the spectrum must be truncated. In order to minimally degrade the resolution by truncating the spectrum, we specify that  $\Delta\Lambda$  and  $\Delta V$  (full end-to-end tuning ranges) are [18]:

$$\Delta\Lambda = \frac{\lambda_c^2\Delta V}{c} = \frac{\pi\Delta\lambda}{2\ln(2)}. \quad (8)$$

Since the iNIRS TOF resolution is inversely related to the tuning range or optical bandwidth, a temporally coherent  $\lambda_c = 855$  nm DFB laser (Eagleyard) with a large mode-hop free tuning range was chosen as the source. The DFB laser is tuned rapidly in wavelength by changing the drive current as illustrated in Fig. 1(b). In contrast to external cavity laser tuning via mechanical elements [19], current tuning is highly stable and repeatable. However, this tuning strategy induces modulation of output power as well, which limits the practical tuning range. The laser free spectral range is already large due to the short DFB cavity length, and the mode hop free tuning range is further extended to a few nanometers by the shift in grating reflectivity achieved by a DFB laser during current tuning. Practically, the current tuning

range is limited by the difference between the maximum allowable forward current (conservatively set to 190 mA because 220 mA is the irreversible damage threshold) and the minimum current required for lasing ( $\sim 30$  mA). A maximal tuning range of  $\Delta\lambda \sim 480$  pm ( $\Delta V \sim 197$  GHz) is then obtained simply from the product of the available current range and a typical wavelength tuning coefficient  $d\lambda/dI = 0.003$  nm/mA for the DFB laser provided by the manufacturer. However, for the particular DFB laser used in this study, a wavelength tuning coefficient of  $\sim 0.002$  nm/mA was measured, limiting the expected tuning range to  $\Delta\lambda \sim 320$  pm (or  $\Delta V \sim 131$  GHz).

In iNIRS, a high tuning speed ( $F_S$ ) is required to measure the electric field faster than the intrinsic decorrelation time scale of the sample. However, the tuning range of DFB lasers is diminished by the transition of the dominant tuning mechanism from thermal to carrier density modulation at fast modulation speeds [20]. This reduces the wavelength tuning coefficient, in turn decreasing the tuning range. To characterize this effect, the tuning range  $\Delta V$  was measured at different tuning speeds [Fig. 2(a)] by analyzing the spectral interference pattern from an MZI with mismatched sample and reference paths. The tuning range is determined as follows:

$$\Delta\lambda = \frac{N_{\text{fringes}} \lambda_c^2}{n\Delta L}. \quad (9)$$

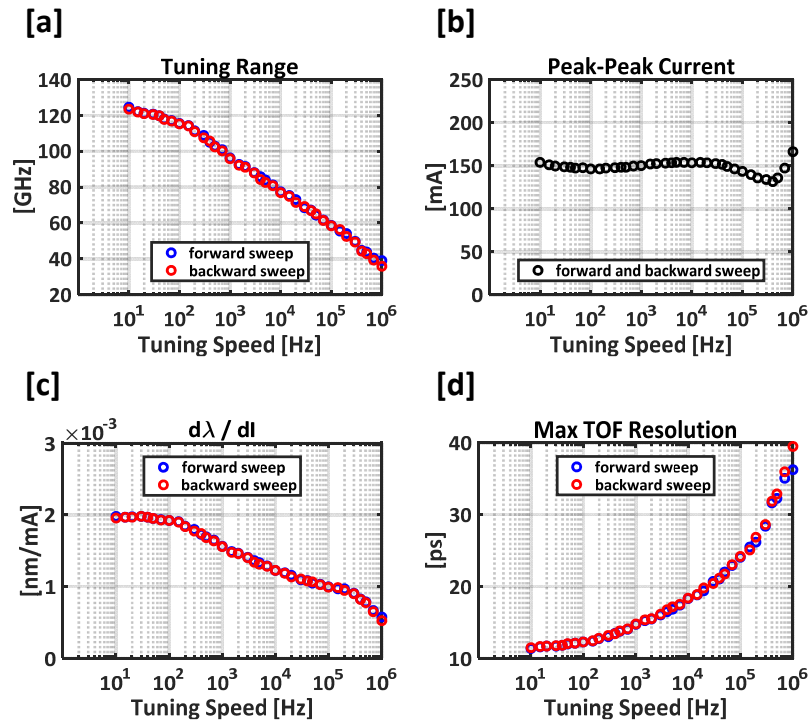


Fig. 2. Current tuning of a distributed feedback (DFB) laser incurs a reduction in tuning range and consequently, TOF resolution, with increased tuning speed. a) Maximal tuning range ( $\Delta V$ ) versus tuning speed. b) Peak-peak current during the sweep. c) Current tuning coefficient ( $d\lambda/dI$ ) versus tuning speed. d) “Max”, or best, achievable time-of-flight (TOF) resolution ( $\delta\tau_s$ ) based on measurements shown in (a) and Eqs. (7) and (8).

Here,  $N_{\text{fringes}}$  represents the number of fringes (obtained from the total deviation of the interference signal’s unwrapped phase divided by  $2\pi$ ),  $n$  is the refractive index of the mismatch medium ( $n = 1.455$  for fiber core), and  $\Delta L = c\Delta\tau_s/n$  is the physical length of the path mismatch between arms. Due to possible filtering in the current controller electronics, input voltage to the controller may not be a reliable indicator of the actual laser drive current

at high tuning speeds. Instead, laser output power was measured by a photodiode. By calibrating the change in photodiode signal to milliamps of current modulation, the photodiode signal was used, indirectly, to infer the drive current [Fig. 2(b)]. The wavelength tuning range divided by the current modulation yielded the wavelength tuning coefficient [Fig. 2(c)]. The decrease in tuning coefficient suggests that thermal tuning becomes less effective with increased tuning speed. As a result, the maximal achievable tuning range is reduced by approximately 53% at  $F_S = 50$  kHz, thence reducing the maximum achievable time-of-flight resolution from 11.5 ps at  $F_S = 10$  Hz tuning speed to nearly 21.7 ps at  $F_S = 50$  kHz tuning speed [Fig. 2(d)].

While a broader tuning range and higher TOF resolution can be achieved by increasing current modulation amplitude, several limitations arise. First, as the maximum forward current ( $I_{\max}$  in Fig. 1(b)) is limited, increasing modulation amplitude requires reducing average current, and therefore, reducing average output power. Second, as the modulation amplitude is increased, energy distributes more asymmetrically across wavelengths in the sweep. In particular, if the drive current approaches the lasing threshold ( $I_{\min}$  in Fig. 1(b)) at shorter wavelengths, power diminishes. Though asymmetries in the spectrum can be compensated numerically, this shaping process incurs a sensitivity penalty, as described in Section 2.5. To better assess this tradeoff between TOF resolution and sensitivity, we investigated both a *high resolution mode* ( $\Delta\lambda = 157$  pm) and a *low resolution mode* ( $\Delta\lambda = 58.6$  pm) at 50 kHz tuning speed.

### 2.3 Tuning speed determines autocorrelation lag time (ALT) resolution

According to DWS [Eq. (6)], the autocorrelation decay rate increases with TOF. As a rule of thumb, we assume that, due to decorrelation during the sweep and sampling considerations, accurate measurement of the decay rate is possible up to TOF values where  $\xi(\tau_s) \sim 1/\delta\tau_d$ , where  $\delta\tau_d$  is the autocorrelation lag time (ALT) resolution. In our previously reported results [12–14], the tuning speed was limited to  $F_S = 50$  kHz, and we employed only forward sweeps, with  $\delta\tau_d = 1/F_S = 20$   $\mu$ s. In order for iNIRS to measure autocorrelations at longer TOFs (corresponding to larger penetration depths), both high sensitivity and lag time resolution (speed) are desired. For *low resolution* and *high resolution mode* at  $F_S = 50$  kHz, we introduced a novel method, described in Section 2.9, to combine forward and backward sweeps to achieve an ALT resolution of  $\delta\tau_d = 1/2F_S = 10$   $\mu$ s, thus using detected photons more effectively. We also investigated a *high speed mode* ( $\Delta\lambda = 62.5$  pm) at  $F_S = 500$  kHz, which achieved an ALT resolution of  $\delta\tau_d = 4$   $\mu$ s due to data transfer limitations, allowing us to investigate the tradeoffs between sensitivity and speed.

### 2.4 Signal processing

In our iNIRS setup, the DFB laser optical frequency is tuned by sinusoidal current modulation, generating both a forward (fwd) and a backward (bwd) sweep. However, optical frequency ( $\nu$ ) is the conjugate variable to TOF ( $\tau_s$ ), and the Discrete Fourier Transform requires uniform sampling [18]. Hence a resampling or interpolation procedure was implemented. The analytic phase of the interference signal as a function of time ( $t$ ) is given by  $\phi(t) = 2\pi\Delta\tau_s\nu(t) + \phi_0$ , where  $\phi_0$  is a phase offset, and  $\Delta\tau_s$  is the known TOF mismatch ( $\Delta\tau_s = 1.25$  ns in Fig. 3). The phase is obtained from the analytic function via Hilbert transformation, a high order polynomial is fitted to it, and all subsequent fringe patterns are interpolated such that the samples are linearly spaced in  $\phi$  (and hence  $\nu$  as well). Note that two distinct solutions for the phase of the analytic function ( $\phi$  and  $-\phi$ ) are possible. The solution with increasing / decreasing phase over time was chosen for the forward / backward sweep, respectively. Given the small tuning range ( $\Delta\lambda \approx 0.1$  nm), linearity in wavelength implies linearity in optical frequency, at least for  $\Delta\tau_s$  up to 100 ns ( $\sim 22$  m). Hence for TOF mismatches of interest, the nonlinearity to be corrected by resampling arises mainly from sinusoidal tuning, and *not* the nonlinear relationship between wavelength and frequency ( $\nu =$

$c/\lambda$ ) [18]. Finally, the interpolated fringe pattern is multiplied by a Hamming window, zero-padded, and inverse Fourier transformed to yield  $\Gamma_{rs}$ . As  $\Gamma_{rs}$  is related to the sample electric field,  $|\Gamma_{rs}|^2$  is related to sample photon number or intensity, and thus  $10\log_{10}(|\Gamma_{rs}|^2) = 20\log_{10}(|\Gamma_{rs}|)$  must be presented on a dB scale.

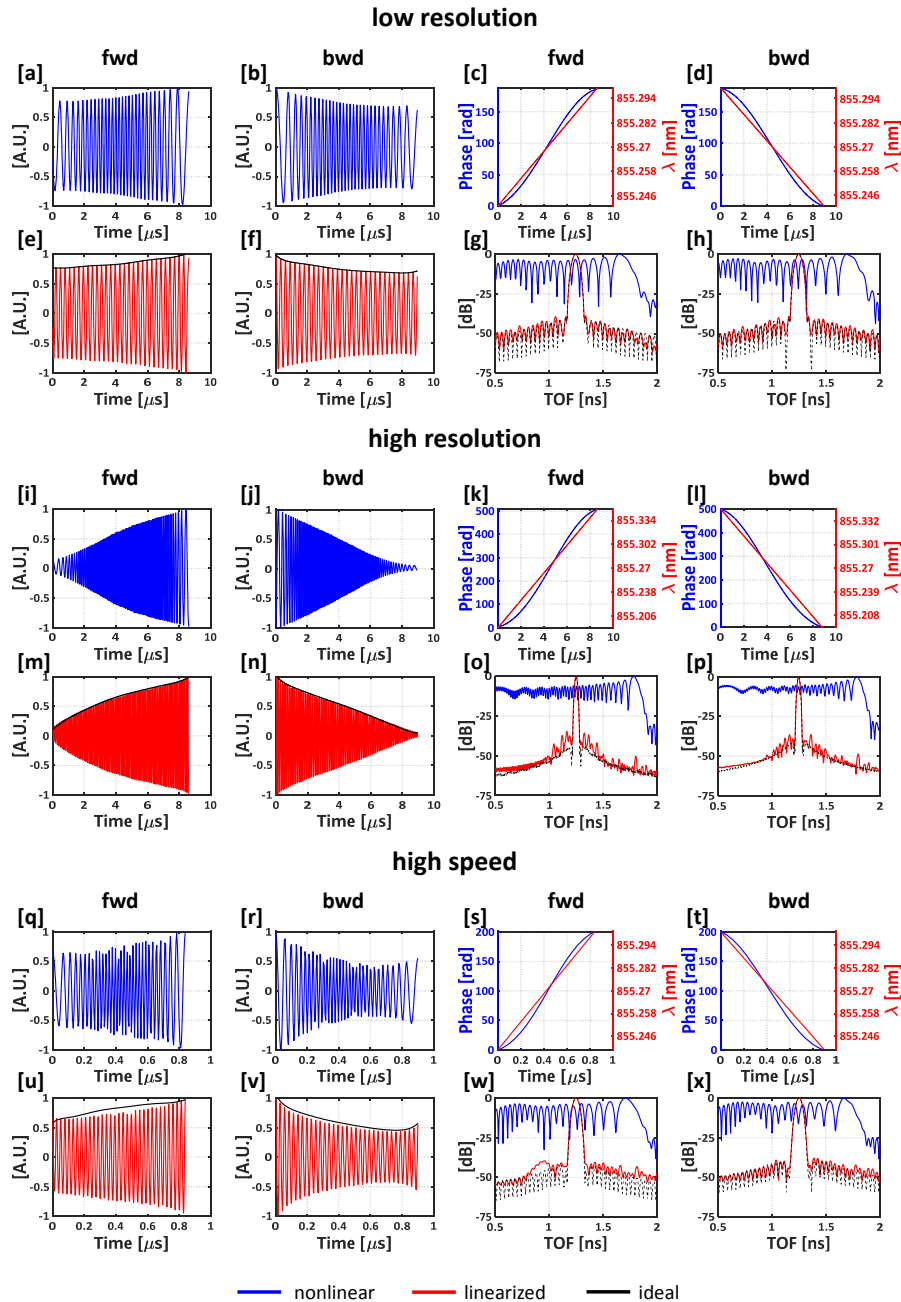


Fig. 3. Interpolation procedure optimizes time-of-flight (TOF) resolution by linearizing interference fringes. Raw mean-subtracted interference signals (a-b, i-j, and q-r). Phase of interference signals before (blue) and after (red) interpolation (c-d, k-l, and s-t). The interpolation procedure linearizes the fringes (e-f, m-n, and u-v) and improves the TOF resolution (g-h, o-p, and w-x), nearly achieving the “ideal” IRF (dotted black) set by the fringe envelopes.

As shown in Fig. 3, interpolation linearizes the phase and dramatically improves TOF resolution (red) relative to no interpolation (blue). To assess whether phase nonlinearity is completely removed by interpolation, an “ideal” IRF can be constructed from the Fourier transform of the resampled and Gaussian shaped fringe envelope (black), thereby defining the TOF resolution achieved with no residual phase error (dotted black). Indeed, this ideal TOF resolution (FWHM  $\approx 60.3$  ps for *low resolution mode*, FWHM  $\approx 22.6$  ps for *high resolution mode*, and FWHM  $\approx 56.7$  ps for *high speed mode*), was achieved for both sweeps (compare red and dotted black lines). As a sanity check, these experimental results are roughly consistent with the theoretical TOF resolutions of  $\delta\tau_s \approx 58.9$  ps for *low resolution mode*,  $\delta\tau_s \approx 22.0$  ps for *high resolution mode*, and  $\delta\tau_s \approx 55.2$  ps for *high speed mode*, determined from Gaussian assumptions in Eqs. (7) and (8). Although the ideal IRF FWHM was achieved for all modes, sidelobes were slightly larger than predicted in *high resolution mode* [Fig. 3(o-p)]. We found that the sidelobes may result from wavelength tuning noise at frequencies above the drive frequency. This problem can be addressed in the future by reducing current controller bandwidth, or additional electronic filtering stages.

### 2.5 Sensitivity

If a single mode fiber is used for light collection in iNIRS, the detection system must use collected photons efficiently. The sensitivity is the minimum transmittance or reflectance that can be measured. As in Fourier domain Optical Coherence Tomography [21], iNIRS uses heterodyne gain to potentially achieve sensitivity limited by shot noise, not detector noise, even though photon counting detectors are not used. Since Fourier domain detection is used [21,22], all detected sample photon paths interfere with the reference path, yielding an efficiency advantage over time-gated NIRS techniques [2,23].

To derive the theoretical shot noise limit for the minimum measurable reflectance or transmittance, we assume that  $N_S$  and  $N_R$  are the number of photons from the sample and reference arms at the detector, respectively, and  $s^2(\nu)$  represents the source spectrum, or density of photons across optical frequency,  $\nu$  [24]. We further assume that  $\int s^2(\nu) d\nu = 1$ . If spectral shaping in the reference and sample arms is negligible,  $S_R(\nu) = N_R s^2(\nu)$  and  $S_S(\nu) = N_S s^2(\nu)$  represent the reference and sample spectral photon densities, respectively. To determine the shot noise limited sensitivity, we write the peak iNIRS signal as

$$\text{signal} = \int \sqrt{S_S(\nu)S_R(\nu)} d\nu = \sqrt{N_S N_R} \int s^2(\nu) d\nu = \sqrt{N_S N_R}. \quad (10)$$

If  $N_S \ll N_R$ , the variance of the noise floor is given by

$$\sigma_{\text{noise}}^2 = \int S_R(\nu) d\nu = N_R \int s^2(\nu) d\nu = N_R, \quad (11)$$

since the detected noise is dominated by Poisson-distributed shot noise from the reference arm. Under these assumptions, the signal-to-noise ratio (SNR) is given by

$$\text{SNR} = \frac{\text{signal}^2}{\sigma_{\text{noise}}^2} = \frac{N_S N_R \left[ \int s^2(\nu) d\nu \right]^2}{N_R \int s^2(\nu) d\nu} = N_S. \quad (12)$$

The number of sample photons at the detector is  $N_S = \alpha \rho_d N_{S,\text{inc}}$ , where  $\alpha$  is the sample reflectance or transmittance,  $\rho_d$  accounts for detector quantum efficiency, and  $N_{S,\text{inc}}$  is the number of incident photons. The sensitivity is the minimum measurable reflectance or transmittance,  $\alpha_{\text{min}}$ , where “measurable” is defined as having an SNR of  $\geq 1$ . Therefore, the shot noise limited sensitivity is

$$\text{sensitivity} = \frac{1}{\alpha_{\text{min}}} = \rho_d N_{S,\text{inc}} = \frac{\rho_d \lambda_e P_S \Delta t}{hc}. \quad (13)$$

Here,  $P_S$  is the time-averaged illumination power over the full sweep in the sample arm,  $\Delta t$  is the acquisition time or sweep duration, and  $h$  is Planck's constant. A notable feature of this expression is that the shot noise limited sensitivity does not depend on the reference power. However, to reach this limit, the reference arm power must be increased so that the shot noise in Eq. (11) dominates detector noise.

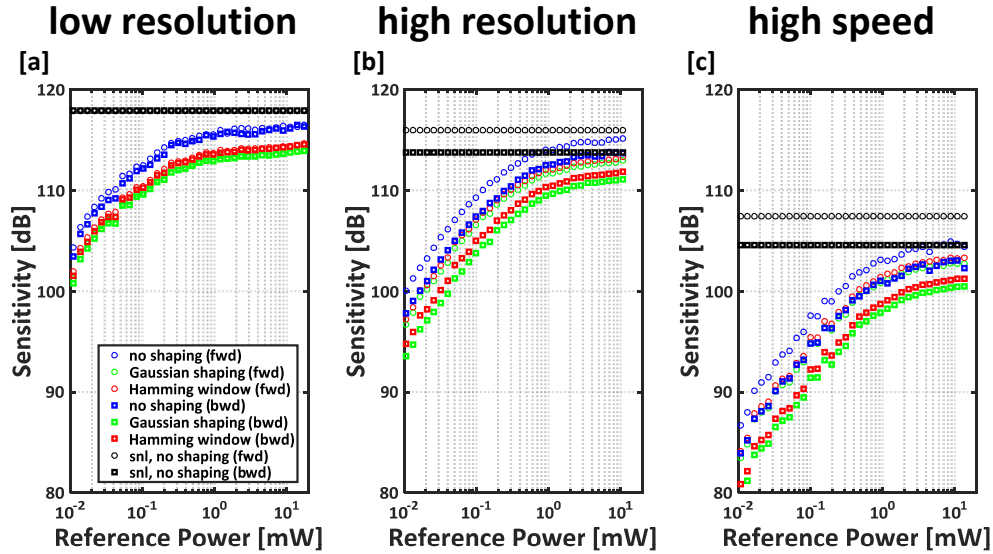


Fig. 4. The iNIRS sensitivity increases with increasing reference arm power and approaches the shot noise limit for both low (a) and high (b) resolution modes, as well as high speed mode (c). The input sample powers were  $P_{S,in} = 35.6$  mW for *low resolution mode*,  $P_{S,in} = 23.2$  mW for *high resolution mode*, and  $P_{S,in} = 29.3$  mW for *high speed mode*. Note that in (a), sensitivities are nearly identical for forward and backward sweeps.

**Table 1. Digital spectral shaping and windowing affect iNIRS sensitivity. The shot noise limit, measured iNIRS sensitivity, and sensitivity loss (difference of previous columns) are provided for all operating regimes. Shaping or windowing methods are color-coded, consistent with other figures.**

Operating Regime	Spectral Shaping Method	Sweep	Shot Noise Limit [dB]	iNIRS Sensitivity [dB]	Loss [dB]
<i>Low resolution</i> ( $F_S = 50$ kHz, $\Delta\Lambda = 58.6$ pm)	no shaping	fwd	117.9	116.5	1.4
		bwd	117.9	116.3	1.6
	Gaussian shaping	fwd	116.0	114.1	1.9
		bwd	116.0	113.9	2.1
	Hamming window	fwd	116.5	114.7	1.8
		bwd	116.6	114.6	2.0
<i>High resolution</i> ( $F_S = 50$ kHz, $\Delta\Lambda = 157.0$ pm)	no shaping	fwd	116.0	115.1	0.9
		bwd	113.7	113.7	0.0
	Gaussian shaping	fwd	114.0	113.0	1.0
		bwd	111.6	111.1	0.5
	Hamming window	fwd	114.6	113.3	1.3
		bwd	112.4	111.8	0.6
<i>High speed</i> ( $F_S = 500$ kHz, $\Delta\Lambda = 62.5$ pm)	no shaping	fwd	107.4	104.4	3.0
		bwd	104.6	102.3	2.3
	Gaussian shaping	fwd	105.6	102.7	2.9
		bwd	102.7	100.5	2.2
	Hamming window	fwd	106.1	103.3	2.8
		bwd	103.2	101.2	2.0

As previously discussed, current modulation for tuning in iNIRS also modulates the spectral shape. This undesirable modulation can be compensated digitally. In order to

determine the effects of digital shaping or windowing on sensitivity, we can add an additional “window” function,  $w(v)$  to Eqs. (10) and (11), yielding

$$\text{signal} = \sqrt{N_s N_R} \int w(v) s^2(v) dv \quad (14)$$

and

$$\sigma_{\text{noise}}^2 = N_R \int w^2(v) s^2(v) dv. \quad (15)$$

Finally, we can determine the sensitivity loss from shaping:

$$\text{sensitivity loss from shaping} = \frac{\left[ \int w(v) s^2(v) dv \right]^2}{\int w^2(v) s^2(v) dv}. \quad (16)$$

This can further be simplified to yield:

$$\text{sensitivity loss from shaping} = \frac{\left[ \int s_w(v) s(v) dv \right]^2}{\int s_w^2(v) dv}, \quad (17)$$

where  $s_w(v) = s(v)w(v)$  describes the windowed, or the “shaped,” spectrum. By the Cauchy-Schwartz inequality, and since  $\int s^2(v) dv = 1$ ,

$$\text{sensitivity loss from shaping} \leq \frac{\int s_w^2(v) dv \int s^2(v) dv}{\int s_w^2(v) dv} = 1, \quad (18)$$

with equality achieved if  $w(v)$  is constant (no shaping). Thus Eq. (17) allows us to calculate the theoretical sensitivity loss from shaping alone, again, assuming the shot noise limit. In reality, the sensitivity loss from shaping may be worse in the presence of detector noise.

The calculated theoretical sensitivities are compared with experimental sensitivities (obtained by attenuating the sample power and measuring the signal-to-noise ratio in direct transmission) in Table 1 for each of the three modes (*low resolution*, *high resolution*, and *high speed*). A quantum efficiency of  $\rho_d = 0.65$  was estimated, and  $\lambda_c = 855$  nm was assumed. The acquisition times are  $\Delta t_{\text{fwd}} = 8.01$   $\mu\text{s}$  and  $\Delta t_{\text{bwd}} = 8.53$   $\mu\text{s}$  for *low resolution mode*;  $\Delta t_{\text{fwd}} = 8.01$   $\mu\text{s}$  and  $\Delta t_{\text{bwd}} = 8.53$   $\mu\text{s}$  for *high resolution mode*; and  $\Delta t_{\text{fwd}} = 0.715$   $\mu\text{s}$  and  $\Delta t_{\text{bwd}} = 0.770$   $\mu\text{s}$  for *high speed mode*. The sample power  $P_s$  is determined for each sweep individually based on the measured average power and ratio of the forward/backward envelope integrals, and taking into account the exclusion of portions of the sweep where the wavelength is stationary. Experimental measurements are compared with theory for all three modes, both with and without windowing/shaping [Fig. 4]. The experimental sensitivity is calculated as the sum of two terms on a dB scale. The first is the maximum value of the intensity, divided by the variance ( $\sigma_{\text{noise,td}}^2$ ) of the complex  $\Gamma_{\text{rs}}$ , measured along delay time ( $\tau_d$ ) and averaged across a small TOF ( $\tau_s$ ) range at the noise floor. The second is the measured attenuation in the sample arm (calculated as the ratio of  $P_{\text{S,in}}$  and  $P_{\text{S,out}}$ , the sample powers before and after attenuation, respectively) in dB:

$$\text{sensitivity} = 10 \log_{10} \left( \frac{|\Gamma_{\text{rs,peak}}|^2}{\langle \sigma_{\text{noise,td}}^2 \rangle_{\tau_s}} \right) + 10 \log_{10} \left( \frac{P_{\text{S,in}}}{P_{\text{S,out}}} \right) \quad (19)$$

In agreement with the theory, we found that for all modes, iNIRS sensitivity increases with reference arm power, approaching a plateau near the shot noise limit [Fig. 4]. Note that sensitivity values vary slightly between forward and backward sweeps due to small

differences in energy between the two sweeps, possibly related to the current controller. The wide plateau in sensitivity at higher reference powers suggests that excess noise does not limit sensitivity. Experimental sensitivity values (measured with 53.3 dB attenuation in the sample arm for *low resolution mode*, 51.6 dB for *high resolution mode*, and 52.5 dB for *high speed mode*) are  $\sim 0$ -3 dB below theoretical values (Table 1). The slight discrepancies between experimental and theoretical sensitivities are attributed to additional system losses that are not accounted for by the detector quantum efficiency ( $\rho_d$ ) alone in Eq. (13), or dynamic range limitations. Finally, we note that an additional 3 dB reduction in sensitivity would be expected from the random polarization of diffuse light from a tissue sample, but is not observed here with direct transmission.

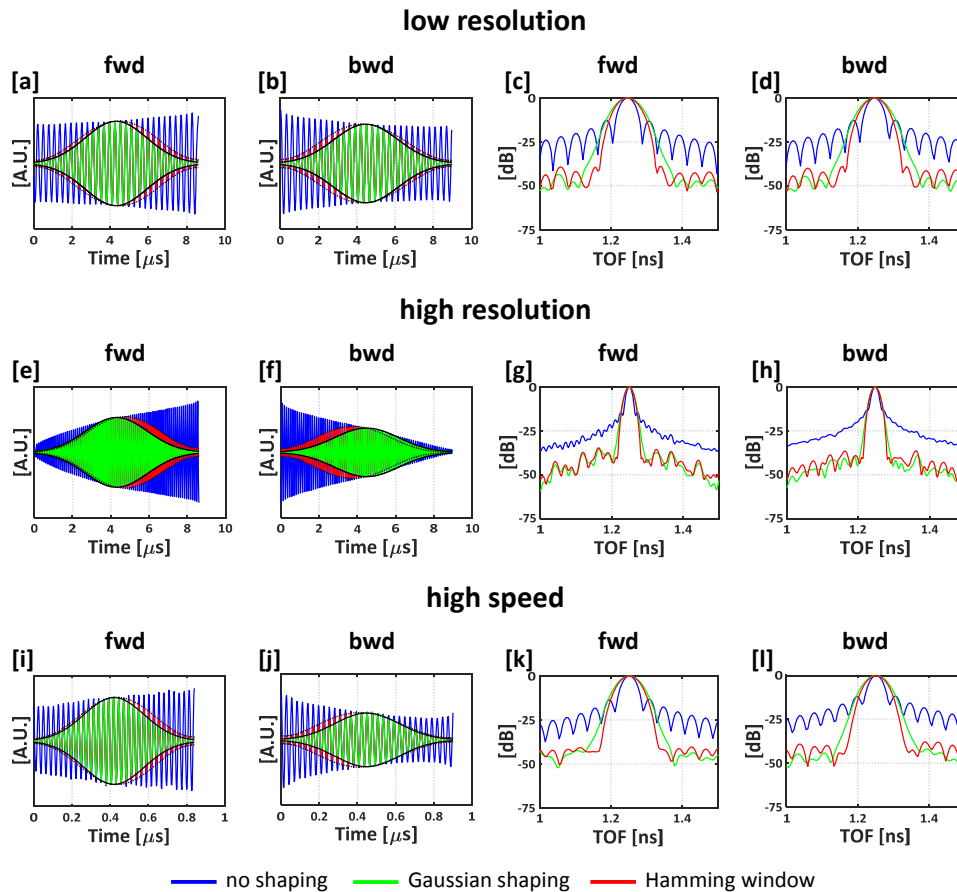


Fig. 5. Impact of Hamming windowing and Gaussian shaping on IRFs (a-d: *low resolution mode*, e-h: *high resolution mode*, i-l: *high speed mode*). Corresponding interference spectra (a-b, e-f, and i-j) and IRFs (c-d, g-h, and k-l) are shown, illustrating a tradeoff between dynamic range (peak-sidelobe ratio) and TOF resolution.

## 2.6 Sampling and time-of-flight range

TOF ranges of nanoseconds or more are needed to measure diffusive DTOFs in iNIRS. The maximum measurable TOF without aliasing ( $\tau_{s,max}$ ) depends on the sampling interval in the optical frequency ( $\nu$ ) domain. In principle, the resampling step could decrease the sampling interval arbitrarily; however, aliasing during data acquisition would still set the maximum measurable TOF. The number of acquired samples in a sweep is  $N_s = \Delta t f_s$ , where  $f_s$  is the digitizer sampling rate (not to be confused with  $F_s$ , the sweep rate) and  $\Delta t$  is the sweep

duration. The maximum measurable TOF is set by the Nyquist limit, given the number of samples ( $N_s$ ) and the tuning range ( $\Delta V$ ). This maximum TOF for a linear sweep can then be related to the TOF resolution ( $\delta\tau_s$ ) as follows:

$$\tau_{s,\max} = \frac{N_s}{2\Delta V} = \frac{\Delta t f_s \delta\tau_s}{2\sqrt{2}}, \quad (20)$$

In our setup,  $f_s = 200$  MS/s; thus, the theoretical maximum measurable TOF values are  $\tau_{s,\max} = 33.4$  ns for *low resolution mode*,  $\tau_{s,\max} = 12.4$  ns for *high resolution mode*,  $\tau_{s,\max} = 2.8$  ns for *high speed mode*. In reality, however, Eq. (20) represents a rough guideline and aliasing may occur for smaller TOFs due to sweep nonlinearity. A more conservative TOF limit is obtained by stipulating that aliasing may not occur at any point during the nonlinear sinusoidal sweep:

$$\tau_{s,\max} = \frac{N_s}{\pi\Delta V} = \frac{\Delta t f_s \delta\tau_s}{\pi\sqrt{2}}. \quad (21)$$

In deriving Eq. (21) we assumed that  $\Delta t$  is the time for half of a full sinusoidal oscillation in wavelength. This more conservative definition yields  $\tau_{s,\max} = 21.3$  ns for *low resolution mode*,  $\tau_{s,\max} = 7.9$  ns for *high resolution mode*,  $\tau_{s,\max} = 1.8$  ns for *high speed mode*. Note that if the electronic detection bandwidth is sufficiently large, ranging may be performed past the limits in Eqs. (20) and (21), if aliasing can be tolerated.

**Table 2. Digital spectral shaping and windowing affect iNIRS TOF resolution and dynamic range. The IRF full-width-at-half-maximum (FWHM), dynamic range (SNR definition), and dynamic range (peak-sidelobe definition) are provided for all operating regimes. Shaping or windowing methods are color-coded, consistent with other figures.**

Operating Regime	Spectral Shaping Method	Sweep	$\delta\tau_s$ FWHM [ps]	Dynamic Range, SNR [dB]	Dynamic Range, Peak-Sidelobe [dB]
<i>Low resolution</i> ( $F_s = 50$ kHz, $\Delta\Lambda = 58.6$ pm)	No shaping	fwd	36.9	67.7	13.1
		bwd	36.5	67.6	12.6
	Gaussian shaping	fwd	60.4	65.3	46.8
		bwd	60.3	64.9	45.3
	Hamming window	fwd	54.1	65.9	42.8
		bwd	53.6	66.0	41.6
<i>High resolution</i> ( $F_s = 50$ kHz, $\Delta\Lambda = 157.0$ pm)	No shaping	fwd	15.5	66.4	14.4
		bwd	16.9	65.0	13.4
	Gaussian shaping	fwd	22.5	64.2	37.4
		bwd	22.7	62.3	39.0
	Hamming window	fwd	22.4	64.7	35.9
		bwd	22.2	63.2	36.4
<i>High speed</i> ( $F_s = 500$ kHz, $\Delta\Lambda = 62.5$ pm)	No shaping	fwd	35.3	53.1	13.4
		bwd	34.2	55.3	11.6
	Gaussian shaping	fwd	56.7	59.6	43.6
		bwd	56.8	57.3	41.8
	Hamming window	fwd	51.8	58.1	40.3
		bwd	50.2	56.8	37.7

## 2.7 Dynamic range

The dynamic range is the ratio of the minimum and maximum signal levels that can be measured at once. One definition of the iNIRS dynamic range is the ratio between the maximum value of the intensity that can be obtained without saturating the detector, and the corresponding noise background variance  $\sigma_{\text{noise},\tau_d}^2$  on a dB scale:

$$\text{dynamic range (SNR)} = 10\log_{10} \left( \frac{|\Gamma_{rs,\text{peak}}|^2}{\langle \sigma_{\text{noise},\tau_d}^2 \rangle_{\tau_s}} \right) \quad (22)$$

The variance is once again measured along delay time ( $\tau_d$ ) and averaged across a small TOF ( $\tau_s$ ) range around the noise floor, as in Eq. (19). In order to quantify the available dynamic range when large and small signals are more closely separated, which is the case at small source-detector separations [25,26], the dynamic range is also quantified by the ratio of the maximum, or peak, intensity, and the intensity of the first sidelobe:

$$\text{dynamic range (peak-sidelobe)} = 10\log_{10} \left( \frac{|\Gamma_{rs,\text{peak}}|^2}{|\Gamma_{rs,\text{sidelobe}}|^2} \right). \quad (23)$$

Since discontinuities at the edges of the interference spectrum can cause sidelobes, apodization and spectral shaping methods can optimize the tradeoffs between sensitivity, TOF resolution, and peak-sidelobe ratio. To this end, in addition to the sensitivity results in Table 1, we demonstrate the impact of Hamming windowing and Gaussian shaping on the dynamic range and time-of-flight resolution [Fig. 5 and Table 2]. The results for both definitions of dynamic range are summarized in Table 2 for all three operating modes.

In practice, the reference power during the dynamic range measurement is increased until it approaches the shot noise limit as determined by Fig. 4, while the sample power is subsequently attenuated to reduce the interference signal to just below saturation. As a result, reference powers were ~4-5.5 mW and sample powers were on the order of 1  $\mu$ W for all regimes. Note that the differential amplifier in the dual balanced detector (Newport 80 MHz Balanced Photoreceiver Model 1807-FC) reaches saturation when the difference in powers between the two inputs reaches 125  $\mu$ W. To achieve a high dynamic range, it is thus imperative that the splitting ratio of the second fiber coupler, shown in Fig. 1(a), is as close as possible to 50:50.

### 2.8 Time-of-flight range

In iNIRS, the TOF range of the system must exceed the extent of the DTOF. Two important determinants of TOF range are the electronic detection bandwidth and dynamic coherence time. For rapidly tunable lasers, the dynamic coherence time is defined by analogy to the coherence time of a laser that is stationary in wavelength. For a wavelength-stationary laser, temporal phase fluctuations ( $\varphi_n$ ) of the light field reduce the interference fringe visibility at large TOF mismatches. Similarly, for a wavelength-swept laser, random phase fluctuations ( $\varphi_n$ ) during a frequency sweep  $\varphi(t) = 2\pi\Delta\tau_s\nu(t) + \varphi_n(t) + \varphi_0$ , reduce the interference fringe visibility at large time delays. In order to characterize this effect, if present, we define the coherence time as the delay in the interferometer at which the visibility of the fringes is reduced to one-half of the visibility at zero delay:

$$\tau_c = \frac{2\ln(2)}{\pi\delta\nu}. \quad (24)$$

Here,  $\tau_c$  is the half-width at half-maximum (HWHM) TPSF measurement range or coherence time, and  $\delta\nu$  is the FWHM of the instantaneous laser linewidth, assumed to be Gaussian. Note that the HFHM coherence length is given by  $L_c = c\tau_c$ .

In swept source OCT, the coherence length is measured experimentally by obtaining interference signals at various path delays sequentially and plotting the point spread function height rolloff versus path mismatch [21]. Alternatively, a method to retrieve the complex electric field of a swept laser was recently introduced, but requires a complicated interferometer setup with multiple detection channels [27]. Here we introduce a simple multi-pass loop method to measure the rolloff of a tunable laser at multiple path mismatches simultaneously. Importantly, to exclude multi-pass losses, the method requires measuring once at a slow tuning rate ( $F_s = 500$  Hz in our experiment), where coherence rolloff and electronic bandwidth effects can be neglected.

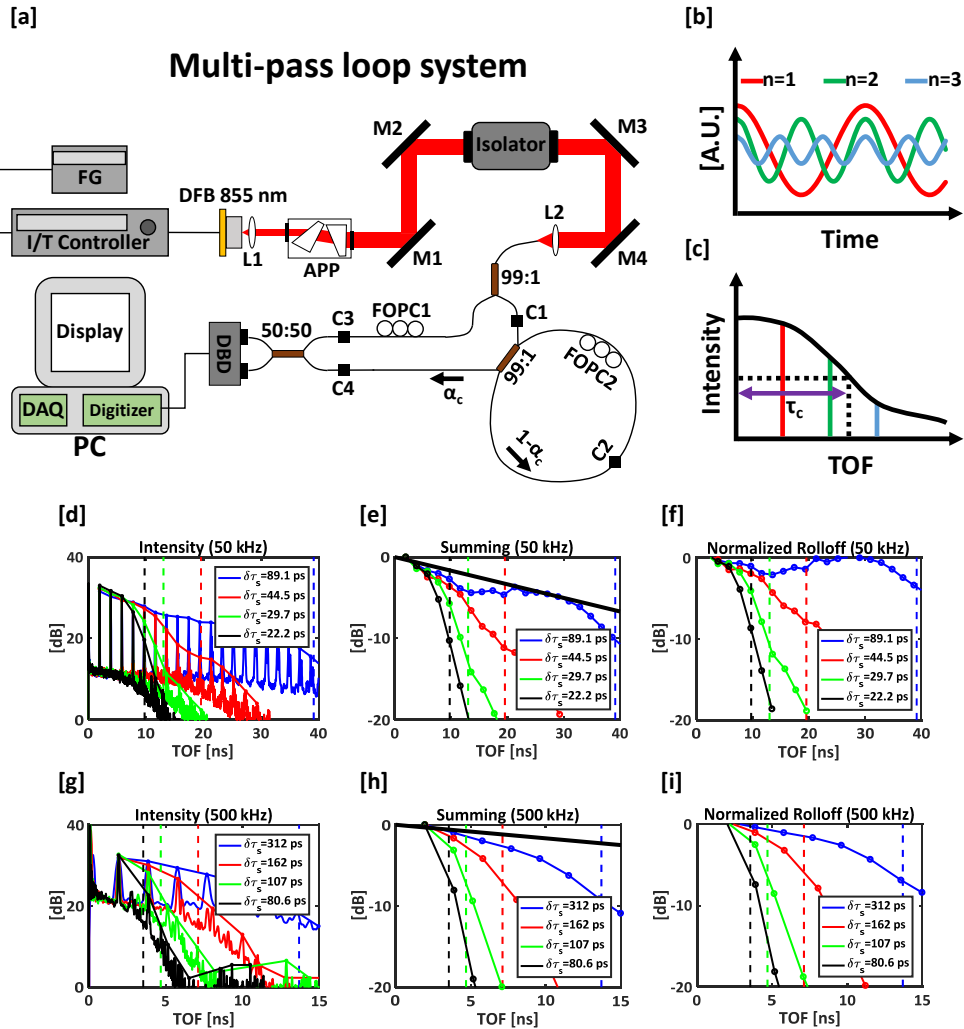


Fig. 6. a) Multi-pass loop method for coherence time measurement of rapidly tunable lasers (DFB – distributed feedback laser, APP – anamorphic prism pair, L1/L2 – lenses, OI – optical isolator, FOPC – fiber optic polarization controller, C1-C4 – FC/APC connections, DBD – dual balanced detector). b) Interference signals are generated for each pass through the loop. c) Without multi-pass losses, Fourier analysis of interference signals yields the rolloff, whose half-width at half maximum is the coherence time ( $\tau_c$ ) of the laser. Loop signals for 50 kHz (d) and 500 kHz (g) tuning rates. The TOF regions around each peak were summed, to mitigate TPSF broadening caused by resampling errors at large TOFs, for 50 kHz (e) and 500 kHz (h) tuning rates. Assuming that the rolloff at a very slow speed of 500 Hz, represented by the bold black line in (e) and (h), is only due to multi-pass losses, normalized rolloffs at higher speeds (50 kHz and 500 kHz) that exclude multi-pass losses can be estimated as the difference in summed rolloffs, (f and i, respectively).

A custom 850 nm, 99:1 fiber coupler with short arms ( $\sim 16$  cm each) was inserted in the reference path of a Mach-Zehnder interferometer. One input and one output FC/APC port of the coupler were connected to form a recirculating loop [Fig. 6(a)]. The multiple passes create a superposition of fringes, where the fringe frequency increases with the number of passes [Fig. 6(b)]. Resampling and Fourier transformation yields a series of peaks with increasing TOF, one for each fringe frequency, where the peak heights are proportional to the fringe amplitudes (corresponding colors in Fig. 6(c)) and peak locations are proportional to the time delay. If the same amount of light were transmitted on each pass, the fringe amplitude would

be proportional to the fringe contrast, and the laser rolloff could be easily determined [Fig. 6(c)]. However, in practice, one must account for multi-pass losses. The output intensity after  $n$  passes through the loop, assuming a coupling ratio of  $\alpha_c$  and a loop transmission of  $\beta$ , which incorporates connector losses, is given by:

$$I_{\text{out}} = \begin{cases} \alpha_c I_{\text{in}} & \text{for } n = 0 \\ \beta^n I_{\text{in}} (1 - \alpha_c)^2 \alpha_c^{n-1} & \text{for } n > 0 \end{cases} \quad (25)$$

Since rolloff may increase with increasing sweep speed due to linewidth broadening and limited electronic bandwidth, we provide measurements at  $F_S = 50$  kHz and  $F_S = 500$  kHz to illustrate tradeoffs at higher speed. Interferograms were acquired once without connecting the loop portion of the interferometer to set baseline IRFs, and then once more with the loop connected so the rolloff was sampled at TOF values equal to multiples of the loop delay. The processed loop signals are presented in Figs. 6(d) and 6(g) for 50 and 500 kHz, respectively. At very large path delays, error in the linearization procedure and phase distortion caused by electronic filtering effects lead to IRF broadening. This is compensated by summing the intensity in regions around each peak [Figs. 6(e) and 6(h)].

Importantly, a measurement at a very slow speed ( $F_S = 500$  Hz) is used to adjust for multi-pass losses. Assuming that laser tuning at  $F_S = 500$  Hz is quasi-static, coherence rolloff effects over the TOF range are negligible (the static DFB laser linewidth is  $\sim 2$  MHz). Moreover, the electronic bandwidth rolloff should be insignificant for TOFs of interest at  $F_S = 500$  Hz. These assumptions are confirmed by fitting a line to the rolloff at 500 Hz (bold black line in Figs. 6(e) and 6(h)) which yields a loss of 0.17 dB/ns, or 0.28 dB/pass, consistent with the expected FC/APC connector loss at C4 ( $\beta \sim 0.2$  dB) and the coupling ratio ( $\alpha_c \sim 0.99$  or  $\sim 0.0436$  dB). Finally, the summed intensity rolloffs are normalized by the rolloff fit at  $F_S = 500$  Hz. Thus, Figs. 6(f) and 6(i) most accurately represent the rolloff of the iNIRS system itself, excluding losses in the multi-pass loop.

In addition to temporal coherence of the laser, filtering in the photodiode or subsequent electronics may further reduce the TOF range. The required electronic frequency bandwidth ( $\Delta f$ ) for sinusoidal wavelength tuning is approximately

$$\Delta f \cong \frac{\pi c \Delta \Lambda F_S \Delta \tau_s}{\lambda_c^2} \quad (26)$$

The electronic bandwidth ( $\Delta f$ ) of the dual balanced detector is 80 MHz, suggesting that increasing TOF resolution (increasing  $\Delta \Lambda$ ) will reduce the TOF mismatch  $\Delta \tau_s$  corresponding to the detection bandwidth limit. This TOF value is represented as a dashed line in Figs. 6(d)-6(i) for various levels of  $\delta \tau_s$  to illustrate the tradeoff between TOF resolution and TOF range.

Investigation of Figs. 6(d)-6(i) suggests that the rolloff is determined by the electronic detection bandwidth, not coherence effects in the laser, at least under our experimental conditions. These results suggest that  $\tau_c \approx 7$  ns at the highest possible TOF resolution of  $\delta \tau_s = 22.2$  ps at 50 kHz, which is much larger than the expected DTOF duration (typically a couple of nanoseconds [2]), and  $\tau_c \approx 3$  ns for a TOF resolution of  $\delta \tau_s = 80.6$  ps at 500 kHz. Furthermore, the slope of the rolloff was always much lower than the asymptotic slope of a typical diffusive DTOF ( $\sim 25$  dB/ns) [28]. Finally, the rolloff can be compensated numerically, if known *a priori*, though the associated sensitivity loss cannot be recovered. Balanced detectors with higher bandwidth and a digitizer with a higher sampling rate will further improve the iNIRS rolloff in the future.

## 2.9 Combining forward and backward sweeps

As discussed above, the choice of iNIRS operating regime involves tradeoffs between various system parameters. Here we show that coherently combining forward and backward sweeps

can improve autocorrelation lag time (ALT) resolution, with no other tradeoffs. To achieve this, the interference fringes for both sweeps, measured over time by the dual-balanced photodetector, must be assigned to the correct optical frequencies ( $\nu$ ) by the resampling procedure. Also, the spectral envelopes must be identical for both sweeps prior to inverse Fourier transformation. Provided these conditions are met, forward and backward sweeps can be successfully integrated in iNIRS analysis. In practice, the unwrapped phase (and optical frequency) during the sweep is obtained via the analytic function of a spectral interference pattern, usually acquired in transmission mode with a known path mismatch. As described in Section 2.4, we assign increasing phase (and frequency) to the forward sweep, and decreasing phase (and frequency) to the backward sweep. Though a sinusoidal drive is used, the actual laser tuning is slightly asymmetric, but highly repeatable. Hence the transition between sweeps was determined as the locally symmetric folding point of the fringe pattern. The unwrapped phase of the analytic function is inaccurate near the edges of the sweep where the phase and frequency are stationary. However, this error was determined through simulations to be  $<1$  radian for TOF values of interest.

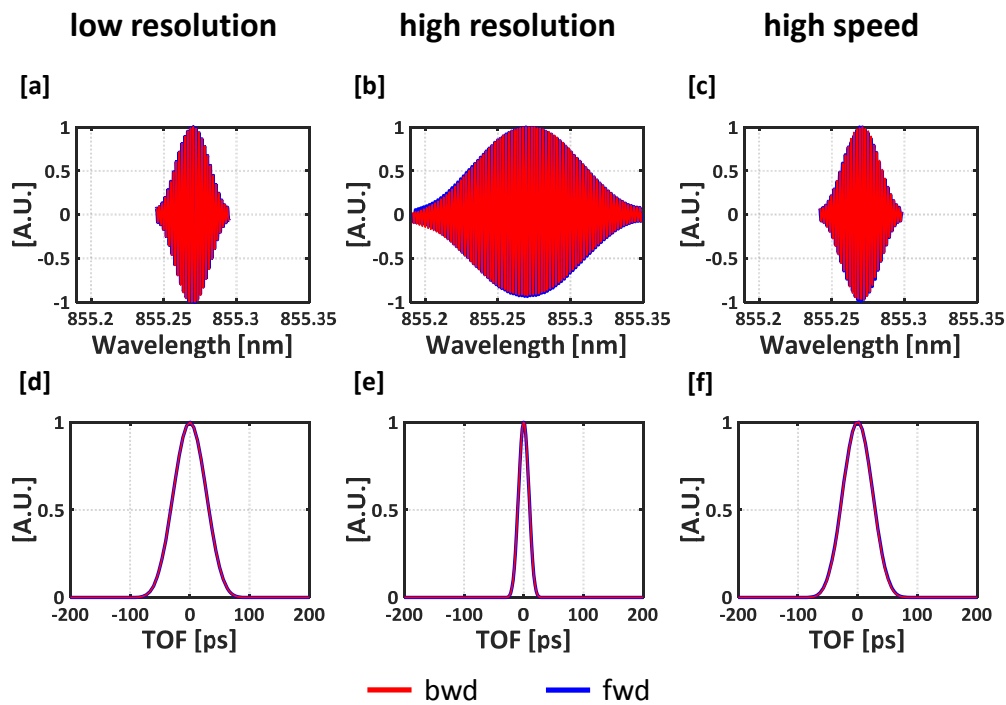


Fig. 7. a-c) Envelopes and fringe frequencies are nearly identical for forward and backward sweeps prior to inverse Fourier transformation. d-f) Resulting forward and backward sweep IRFs show good agreement.

After each point in both forward and backward sweeps was assigned to an optical frequency, both sweeps were interpolated to achieve linear sampling in  $\nu$ . Next, both sweeps were digitally shaped to achieve the same spectral envelope, as shown in Figs 7(a)-7(c). Finally, after inverse Fourier transformation, the residual phase shift between the forward and backward sweep was corrected, and the two were intercalated to form a new  $\Gamma_{rs}(\tau_s, t_d)$  time series with twice the temporal ( $t_d$ ) resolution. A comparison of IRFs derived from either forward sweeps or backward sweeps is shown in Figs. 7(d)-7(f). The autocorrelation  $G_1^{\text{iNIRS}}(\tau_s, \tau_d)$  was estimated as described previously [13], treating data from both sweeps identically. This procedure has the advantage of being both simple and unbiased. However, as

forward and backward sweeps had slightly different signal-to-noise ratios (Table 1), a weighted autocorrelation estimate may improve results in the future.

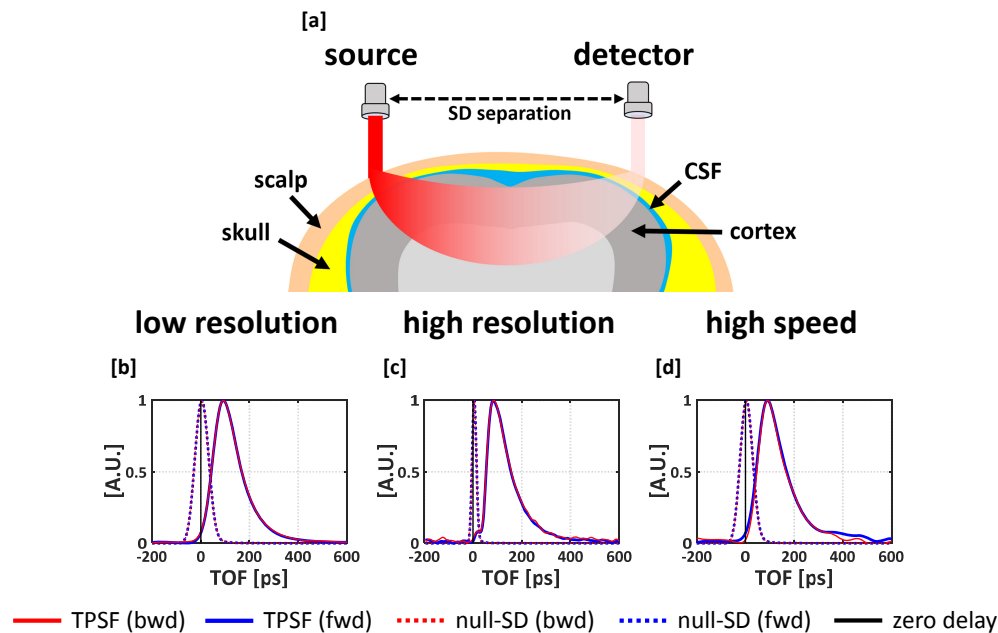


Fig. 8. a) iNIRS was performed noninvasively in the nude mouse brain *in vivo* in reflectance mode. (b-d) *In vivo* TPSFs at null (dashed blue/red) and 7.6 mm (solid blue/red) source-detector separations. The solid black vertical line in b-d represents the zero TOF position as determined by the centroid of the null SD TPSF.

### 3. *In vivo* results

The iNIRS optimizations described in Section 2 were tested *in vivo* in the nude mouse brain. After anesthesia induction, a male nude mouse (SKH-1E, Charles River) was immobilized in a stereotactic frame with a ventilating system supplying 1.2% v/v isoflurane in medical air. Contact-free measurements were performed at a source-detector (SD) separation of 7.6 mm and at null SD separation, for all three modes: *low resolution*, *high resolution*, and *high speed*. Figure 8(a) displays a cartoon of the reflectance geometry. The zero TOF position for TPSFs is approximately the centroid of the null SD reflectance TPSF, with the caveat that the centroid of the null SD TPSF is slightly biased towards longer TOFs by scattering. Therefore, all TPSFs were delayed by an additional 6 ps (estimated by Monte Carlo simulation) to correct this bias. The IRF was measured in transmission geometry. The resulting null SD and 7.6 mm SD TPSFs are displayed in Figs. 8(b)-8(d). Note that the forward and backward sweeps overlap for all SD separations and modes, supporting the consistency of the processing method for forward and backward sweep TPSFs.

#### 3.1 Mouse brain optical properties

As forward and backward sweeps yielded consistent TPSFs [Fig. 8], they were averaged to improve signal-to-noise ratio, and re-normalized by the maximum value. Optical properties were then determined by fitting with diffusion theory. The forward and backward sweep TPSFs were determined individually and averaged [Eq. (1)], and then fitted with  $A \times \mathfrak{R}(\tau_s) * \text{IRF}(\tau_s)$  as described by Eq. (3); the fitting results are shown in Fig. 9 and Table 3.

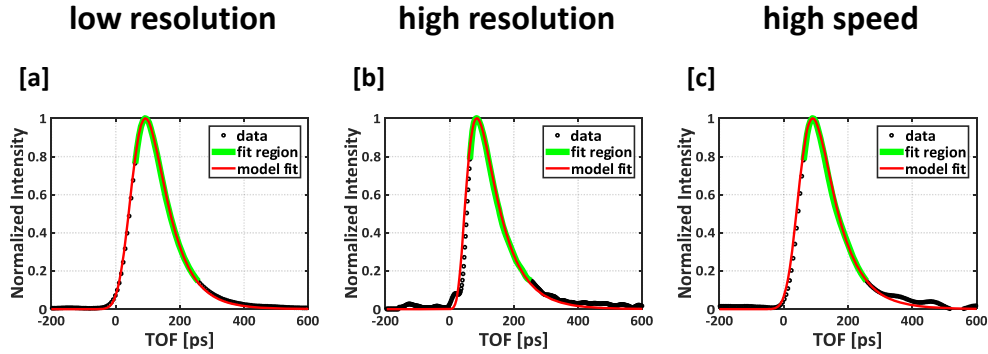


Fig. 9. a-c) TPSFs (black circles) are fitted with diffusion theory (red). The fitting window is highlighted green. Corresponding *in vivo* mouse brain optical properties are shown in Table 3.

**Table 3. Extracted optical properties of the *in vivo* mouse brain. For the three operating regimes, the extracted optical properties, the 95% confidence interval (CI), and the mean squared error (MSE) are provided.**

Operating Regime	Absorption, $\mu_a$ [95% CI]	Reduced Scattering, $\mu_s'$ [95% CI]	MSE
<i>Low resolution</i> ( $F_s = 50$ kHz, $\Delta\lambda = 58.6$ pm)	$0.49 \text{ cm}^{-1}$ [0.47-0.51]	$12.7 \text{ cm}^{-1}$ [12.3-13.1]	0.000068
<i>High resolution</i> ( $F_s = 50$ kHz, $\Delta\lambda = 157.0$ pm)	$0.43 \text{ cm}^{-1}$ [0.42-0.45]	$11.0 \text{ cm}^{-1}$ [10.7-11.3]	0.000161
<i>High speed</i> ( $F_s = 500$ kHz, $\Delta\lambda = 62.5$ pm)	$0.43 \text{ cm}^{-1}$ [0.40-0.46]	$11.9 \text{ cm}^{-1}$ [11.3-12.5]	0.000194

The fitting window starts at a TOF value that corresponds to  $\sim 80\%$  of the peak, and ends when the signal drops to  $\sim 15\%$  of the peak (highlighted in green in Fig. 9). The extracted optical properties are summarized in Table 3. The 95% confidence intervals of the measurements do not overlap: discrepancies may be attributed to the fact that TPSFs were acquired  $\sim 10$  minutes apart, and possible decorrelation during the sweep for the *low resolution mode*. Yet, all recovered optical properties are consistent with spatial frequency domain imaging literature values for the mouse brain *in vivo* [29,30].

### 3.2 *In vivo* optical field autocorrelations

To validate the procedure for combining mutual coherence functions from forward and backward sweeps in a single coherent time series (Section 2.9) field autocorrelations were normalized, after noise correction [9], as follows:

$$g_1^{\text{iNIRS}}(\tau_s, \tau_d) = \frac{G_1^{\text{iNIRS}}(\tau_s, \tau_d)}{G_1^{\text{iNIRS}}(\tau_s, 0)}. \quad (27)$$

By intercalating mutual coherence function data from both sweeps into a single time series (Section 2.9), a lag time resolution of  $\delta\tau_d = 1/2F_s = 10 \mu\text{s}$  was achieved at  $F_s = 50$  kHz [Fig. 10]. This was better than  $\delta\tau_d = 1/F_s = 20 \mu\text{s}$  demonstrated previously [14]. For validation, by including mutual coherence function data from corresponding unidirectional sweeps (either forward or backward) in alternating cycles ( $F_s = 500$  kHz) in the time series, a lag time resolution of  $\delta\tau_d = 2/F_s = 4 \mu\text{s}$  was achieved [Fig. 10]. Despite differences in the iNIRS operating parameters and lag time resolution, the normalized optical field autocorrelations are consistent. Slight discrepancies may be caused by physiological fluctuations between measurements, or differing TOF resolutions between the different modes.

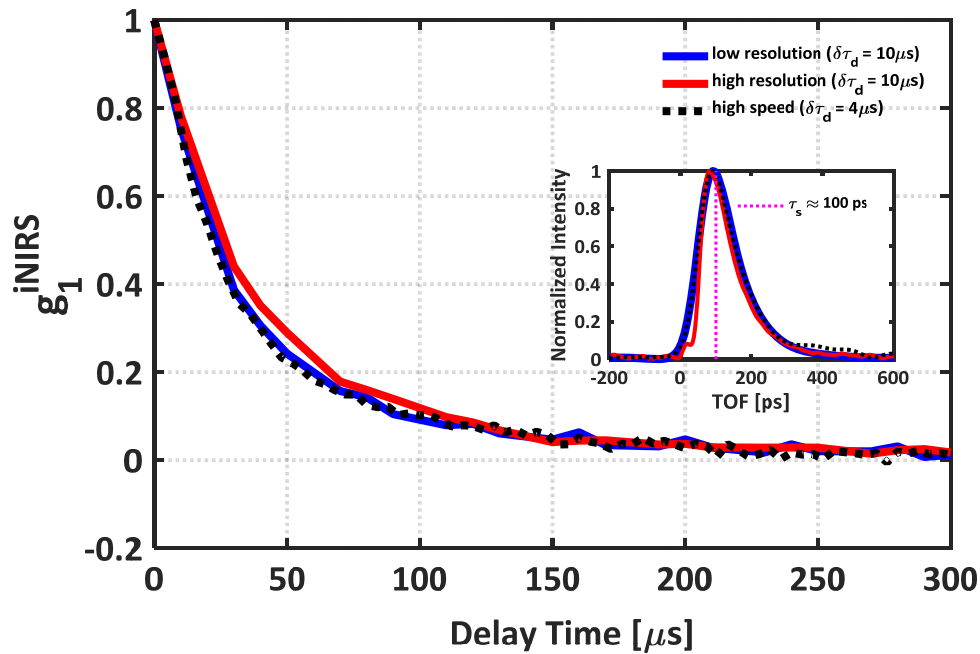


Fig. 10. Normalized optical field autocorrelations for all modes approximately agree at a time-of-flight of  $\tau_s \approx 100$  ps. Note that autocorrelations with  $\delta\tau_d = 10 \mu\text{s}$  are derived from coherent comparisons of bidirectional (forward and backward) sweeps at 50 kHz, while autocorrelations with  $\delta\tau_d = 4 \mu\text{s}$  are derived from unidirectional sweep comparisons only.

#### 4. Discussion

This work comprehensively describes the tradeoffs in an interferometric near-infrared spectroscopy (iNIRS) system that uses a current tuned distributed feedback (DFB) laser. While some tradeoffs are fundamental to the iNIRS method, others are particular to the laser and tuning mechanism used in this study. Here, we summarize the major performance tradeoffs, comment on their relevance to other tunable laser technologies, and point the way towards future system improvements.

##### 4.1 TOF resolution vs. tuning rate

Because current tuning of the DFB laser does not involve mechanical elements [Fig. 1], tuning is stable and repeatable. However, current tuning is limited by the switch from thermal to carrier density modulation at fast modulation speeds [20]. The resulting degradation of tuning coefficient with tuning rate results in the observed loss of TOF resolution [Fig. 2], because, as per Eq. (7), TOF resolution is inversely proportional to the tuning range. While the dynamic tuning range approaches the quasi-static limit at slow tuning rates, the maximum tuning range decays at a rate of  $\sim 20$  GHz/decade beyond a few kHz tuning rate [Fig. 2(a)]. Therefore, the achievable TOF resolution  $\delta\tau_s$  increases from 11.5 ps at 10 Hz to nearly 40 ps at 1 GHz [Fig. 2(d)]. Although the fitting procedure to determine  $\mu_a$  and  $\mu_s'$  [Eq. (3)] does account for the finite TOF resolution, worse TOF resolution may increase uncertainty in the two fitted parameters in the presence of noise. Nevertheless, TOF resolutions achieved by iNIRS are competitive with or better than state-of-the-art time-domain systems [31]. To explicitly use the non-diffusive information at early TOFs, higher TOF resolutions are desired. TOF resolution could be improved by a DFB laser with a higher current tuning coefficient, which can reach 0.02 nm/mA albeit with lower output power [32], or alternative lasers with different tuning mechanisms.

#### 4.2 TOF resolution vs. sensitivity

We showed that iNIRS approaches the shot noise limit [Fig. 4], where the sensitivity is proportional to the number of photons incident on the sample. As the sample power (photons incident per unit time) was limited by the laser output power in this study, the maximum achievable sensitivity was also limited by the maximal laser output power.

When current tuning the DFB laser, variation of the injection current changes not only the optical wavelength, but also the gain, and therefore, the optical power. The tradeoff between TOF resolution and sensitivity arises from this concomitant modulation of the laser output power [Fig. 1(b)]. Low TOF resolution needs a low tuning range,  $\Delta\lambda$ , which requires only a small current modulation; thus the central current  $I_c$  can be increased. In the limiting case where  $\Delta\lambda$  is infinitesimally small, the central current could be raised all the way to maximum current ( $I_{\max}$ ). Note that the additional digital spectral shaping required for a wider sweep incurs an additional sensitivity penalty, as per Eq. (17). Consequently, by going from a high to low TOF resolution, the shot noise limit described by Eq. (13) can be increased by  $>3$  dB. The tradeoff between TOF resolution and sensitivity is summarized by Fig. 4 and Table 1.

Finally, the resolution-sensitivity tradeoff, arising from undesired power modulation of the laser, can be circumvented by other laser tuning mechanisms which decouple the tuning of wavelength selectivity from injection current to the active gain region [33,34]. For tunable lasers where the output power is below the American National Standards Institute (ANSI) limit, optical amplification techniques can be considered as well.

#### 4.3 Number of resolvable TOFs vs. tuning rate

A tradeoff between the number of resolvable TOFs (the TOF range  $\tau_{s,\max}$  divided by the TOF resolution  $\delta\tau_s$ ) and tuning rate  $F_S$  can arise from the limited sampling rate, limited detection bandwidth, and possible coherence effects in the laser. The sampling rate limitation is described in Eq. (21), which expresses the requirement that aliasing does not occur at any point during a sinusoidal sweep. The detection bandwidth limitation is described in Eq. (26) and was demonstrated experimentally in Fig. 6 using a multi-pass loop. Both equations can be summarized succinctly as  $(\tau_{s,\max}/\delta\tau_s)F_S \sim f_s$  (sampling rate), and  $(\tau_{s,\max}/\delta\tau_s)F_S \sim \Delta f$  (bandwidth), where  $\tau_{s,\max}/\delta\tau_s$  is the number of resolvable TOFs. These tradeoffs can be ameliorated by increasing the digitizer sampling rate  $f_s$  and detection bandwidth  $\Delta f$ , respectively. Finally, though experimental rolloffs in Fig. 6 can be attributed to the limited 80 MHz detection bandwidth, our multi-pass loop approach can also be used to characterize degradation in instantaneous coherence length as well. This may be expected for faster wavelength tuning (i.e. more nanometers per second), or different tunable source technologies.

#### 4.4 Tuning rate vs. sensitivity

We showed that shot noise limited sensitivity in iNIRS is nearly achieved for all modes [Fig. 4], though higher loss at 500 kHz may suggest the presence of excess noise [Table 1]. If the average incident sample power is limited by ANSI exposure limits [35], at higher tuning rates, the sensitivity for a single sweep decreases due to the decrease in sweep photon number. To partially offset this tradeoff, here we demonstrated combination of forward and backward sweeps, essentially doubling the autocorrelation lag time resolution and using detected photons more effectively, with no associated tradeoffs. It should also be noted that if coherent averaging of multiple shot noise limited sweeps is performed, the sensitivity can be theoretically recovered [36].

#### 4.5 Dynamic range

System dynamic range is particularly important in time-resolved measurements at short source-detector separations where backscattered and few-scattered light reaches the detector [25,26]. A high system dynamic range is needed so that these early paths do not obscure more

deeply penetrating, diffuse light paths. Here we characterize the tradeoffs between dynamic range and sensitivity and TOF resolution via digital spectral shaping or windowing methods (Tables 1 and 2), achieving peak-sidelobe ratio dynamic ranges of ~36-47 dB. In particular, Gaussian shaping improves the peak-sidelobe ratio dynamic range, with a minor penalty in sensitivity and TOF resolution. iNIRS achieves considerably cleaner IRFs and better peak-sidelobe dynamic ranges (up to >45 dB) than time-domain NIRS systems (~20-25 dB peak-sidelobe dynamic range) [37–39], which are susceptible to afterpeaks and afterpulses (PMTs) [40] or diffusion tails (SPADs) [38,39]. Such non-uniformities in the IRF severely contaminate information from deep structures [39]. Yet, time-domain NIRS systems can achieve slightly better SNR dynamic ranges (~70 dB) [37] than iNIRS (~57-66 dB with shaping or windowing).

#### 4.6 Comparison with existing techniques and future directions

This work explores optimization of an iNIRS system for measurements of tissue optical and dynamical properties. Currently, iNIRS fills a mesoscopic niche between microscopic (Optical Coherence Tomography) and macroscopic (time-domain NIRS) systems. Though single mode fibers are used in iNIRS, shot noise limited sensitivity is nearly achieved. Thus iNIRS can be expected to achieve similar effective photon count rates as diffuse correlation spectroscopy (DCS) with polarized detection [5], which also uses single mode fibers [41].

The TOF range of iNIRS is already sufficient to measure nanosecond-scale DTOFs [Fig. 6]. Therefore, it is appealing to speculate on applying iNIRS to the adult human brain. The autocorrelation lag time resolution of  $\delta\tau_d = 4 \mu\text{s}$  currently enables measuring an exponential autocorrelation decay rate of up to  $1/\delta\tau_d = 1/4 \mu\text{s}^{-1}$ , which approaches values needed for the adult human brain. However, a lag time resolution of  $\delta\tau_d = 1 \mu\text{s}$  would be more desirable for deep brain sensitivity. This will be achievable at the laser tuning rate of  $F_s = 500 \text{ kHz}$  demonstrated here, with improved data acquisition. For iNIRS to be competitive with time-domain NIRS, further improvement in light collection by incorporating multiple detectors is needed [42]. Additional improvement may also be achieved by reducing the source detector separation in the future, taking advantage of the demonstrated high TOF resolution and dynamic range to maintain depth sensitivity [25].

## 5. Conclusion

In summary, we have characterized key iNIRS system parameters including tuning rate, sensitivity, dynamic range, TOF resolution, and TOF range. We showed that our distributed feedback laser iNIRS system approaches the shot noise limit, and can achieve a dynamic range (peak-sidelobe ratio) of >45 dB. In addition, we introduced a novel multi-pass method to assess the TOF measurement range of our system, concluding that it is limited by electronic detection bandwidth, not intrinsic laser coherence effects, under typical operating conditions. Finally, we demonstrated a method to coherently combine forward and backward sweeps, doubling the temporal sampling and using detected photons more effectively, with no associated tradeoffs. We demonstrated the self-consistency of iNIRS TPSFs and autocorrelations *in vivo* at a variety of tuning rates and TOF resolutions. The methods of characterization and benchmarks presented here lay the groundwork for assessing the performance of future interferometric sensing systems that use rapidly tunable lasers.

## Funding

National Institutes of Health (NIH) (R01NS094681 and R21NS105043).

## Acknowledgments

We would like to thank Conrad Merkle and Marcel Bernucci for helping with animal preparation, and thank Dr. Shau Poh Chong and Dr. Michael Radunsky (Vescent Photonics) for general advice.